ELSEVIER

Contents lists available at ScienceDirect

Atmospheric Research

journal homepage: www.elsevier.com/locate/atmosres





Lightning radiometry in visible and infrared bands

Jacob Wemhoner ^a, Lydia Wermer ^b, Caitano L. da Silva ^{a,*}, Patrick Barnett ^b, Cameron Radosevich ^b, Sonal Patel ^b, Harald Edens ^c

- ^a Department of Physics and Langmuir Lab, New Mexico Tech, Socorro, NM 87801, USA
- ^b Sandia National Laboratories, Albuquerque, NM 87123, USA
- ^c Los Alamos National Laboratory, Los Alamos, NM 87545, USA

ARTICLE INFO

Keywords: Lightning Radiometry Photometry Thunderstorm Optical radiation Radiative transfer

ABSTRACT

Calibrated measurements of lightning optical emissions are critical for both quantifying the impacts of lightning in our atmosphere and devising detection instruments with sufficient dynamic range capable of yielding close to 100% detection efficiency. However, to date, there is only a limited number of investigations that have attempted to take such calibrated measurements. In this work, we report the power radiated by lightning in both visible and infrared bands, assuming isotropic emission, and accounting for atmospheric absorption. More precisely, we report peak radiated power and total radiated energy in the combined visible plus near-infrared range (VNIR, 0.34–1.1 μ m), around the H_a line (652–667 nm), and for the 2–2.5 μ m infrared band. The estimated peak power and total energy radiated by negative cloud-to-ground return strokes in the VNIR range is 130 MW and 20 kJ, respectively. Additionally, we detected peak radiated powers of 12 and 0.19 MW in the H_{α} and infrared bands, respectively. We cross-reference the optical data set with peak current reported by a lightning detection network. The resulting trend is that optical power emitted around the H_{α} line scales with peak return stroke current according to a power law with exponent equal to 1.25. This trend, which should be approximately true across the entire visible spectrum, can be attributed to the plasma negative differential resistance of the lightning return stroke channel. We conclude by discussing the challenges in performing calibrated measurements of lightning optical power in different bands and comparing the results with previously-collected data with different experimental setups, observation conditions, and calibration methods.

1. Introduction

Photodiodes offer a unique way to view optical phenomena as they can provide both luminosity and optical power measurements radiated by rapid processes, such as the lightning return stroke, which traverses the atmosphere at a fraction of the speed of light in a vacuum. The use of calibrated photodiodes to measure optical power is called radiometry, and this technique has helped the lightning research community quantify the amount of energy radiated by lightning in the visible range (Krider et al., 1968; Guo and Krider, 1982; Paxton et al., 1986; Krider, 1992). These studies cross-referenced the radiated power measurements in both the early stages and late stages of the return stroke with laboratory spark experiments, computational simulations, and mathematical models. In addition, integration of previous high-speed streak photography measurement also verified the early-stage photodiode data (Jordan and Uman, 1983). Photodiodes are still in use due to their capability

of responding well to extremely high sampling rates. Their main disadvantage is that they integrate the optical luminosity in the entire field of view, which makes it difficult to retrieve the source spatial dynamics, or to isolate a particular physical process. This can be alleviated by looking at the irradiance of a small channel section during rockettriggered lightning (Quick and Krider, 2017). Recently, Carvalho et al. retrieved the spatiotemporal dynamics of triggered lightning return strokes by stacking up an array of photodiodes (Carvalho et al., 2014; Carvalho et al., 2015; Carvalho et al., 2018).

The most recent investigations into optical power using photodiodes were done by Quick and Krider (2013); Quick and Krider, 2017 for both natural and rocket-triggered lightning. Their 2013 article is focused on natural lightning and uses a broadband visible photodiode that is similar to the one used in this investigation, with approximate uniform response in the visible plus near-infrared ranges (0.4–1 μm), hereafter referred as the VNIR range. By assuming isotropic emission with no atmospheric

E-mail address: caitano.dasilva@nmt.edu (C.L. da Silva).

^{*} Corresponding author.

absorption, Quick and Krider (2013) reported mean values for peak radiated power and total emitted energy for negative and positive flashes to ground, and for VNIR pulses associated with intracloud (IC) discharges. Negative cloud-to-ground (-CG) flashes were further discriminated into 3 categories: first strokes, subsequent strokes with a new ground connection, and subsequent strokes that re-illuminated a preexisting channel. For -CG flashes they reported median radiated power values of 18, 11, and 4 GW, and total emitted energies of 3.6, 3.5, and 1.2 MJ in the three aforementioned categories, respectively. Positive CGs (+CGs) radiated about the same peak VNIR power (19 GW on average), but had higher energy output (9 MJ on average). A comparable peak radiated power was inferred despite +CGs having twice as large average peak currents (43 kA for positive versus - 21 kA for negative first strokes). VNIR light pulses associated with a cloud illumination had lower average amplitudes, of about 3 GW and 1.5 MJ. At first glance, Quick and Krider's article presents an ideal opportunity for comparison with the VNIR values reported here. However, in the Discussion section we spend considerable effort making the case that direct comparisons with Quick and Krider's work are not straightforward, largely due to differences in the detectors.

Infrared data of the lightning return stroke is particularly sparse in the literature. The main results in the community were obtained with high-speed photography using a FLIR camera and were only published recently (Ding et al., 2020; Ding et al., 2021; Ding and Rakov, 2022). These papers focus their investigation on negative-lightning stepped leaders and provide broadband (3–5 μm) infrared measurements with relative intensity. Without proper calibration, high-speed cameras can only provide relative intensity measurements. But when coupled with a prism or grism, they can provide valuable spectral information. Recent investigations using high-speed spectroscopy in the visible range have quantified the return stroke channel plasma properties with 1.5 μ s temporal resolution (Walker and Christian, 2019; Taylor et al., 2022) and its variation along the channel height (Boggs et al., 2021). However, return stroke spectroscopy was not the subject of Ding et al.'s investigations. These authors used the infrared camera to analyze in detail the physical processes taking place near the tip of negative stepped leaders coming to ground (Ding et al., 2020). To the best of our knowledge, it remains to be determined how much energy a lightning flash emits in infrared. Infrared radiometry is challenging and subject to selecting photodiodes that view within atmospheric transmission windows. Fig. 1 shows the transmission of visible and infrared light through the atmosphere indicating that there are numerous windows where infrared lightning observations are, in principle, possible. This paper focuses on the 2-2.5 µm band, as there are no major atomic and molecular lines in this region and optical transmission is equivalent or better than in the visible range (Laux et al., 1995; Traub and Stier, 1976). Our expectations are that, in the longer term, extending radiometry to infrared bands will improve our understating of lightning processes that take place at plasma temperatures between 5,000 and 20,000 K, i.e., at lower temperatures than the return stroke itself. Some potential applications include: studying the intricate dynamics of plasma decay and reactivation taking place near the leader tip (Ding et al., 2020), ascertaining the presence and role of molecular emissions in leader processes (Kieu et al., 2021), and probing the temporal evolution of the lightning channel temperature based on band-integrated photometric measurements (Pérez-Invernón et al., 2022).

For many years lightning detection from space has been done exclusively in the near-infrared portion of the electromagnetic spectrum (Christian et al., 2003), and has only recently been extended to other bands (Pérez-Invernón et al., 2022). The Geostationary Lightning Mapper (GLM) onboard of the GOES-R satellites observes lightning in a single narrow band around the 777.4 \pm 0.5 nm oxygen triplet line, which has been the standard in the field since its predecessors (Goodman et al., 2013). The Atmosphere and Space Monitor (ASIM) instrument onboard of the International Space Station, on the other hand, has three channels observing at 180–230 nm, 337 ± 2 nm, and 777.4 ± 2.5 nm, respectively (Neubert et al., 2019). Space-based observations are a powerful tool to quantify the effects of lightning in a global scale. But the first step to create a correspondence between optical energies measured from space into the potential impacts of lightning in our atmosphere, is to develop an understanding of the relationship between optical and electrical properties of lightning flashes. Investigations such as the work of Quick and Krider (2013); Quick and Krider, 2017 have paved the way, but are still limited to the VNIR portion of the optical spectrum. In this investigation, we present energy and power estimates in visible and infrared bands. The goals are to augment our research community's knowledge on the power radiated by lightning in the VNIR range and to provide novel estimates of energy emission in the 2-2.5 µm infrared band. The optical recordings are cross-referenced with the Earth Networks Total Lightning Detection Network (ENTLN) data to provide the relationship between emitted power and peak current.

2. Methodology

2.1. Experimental setup

On August 10, 2021, we collected radiometric data from the Langmuir Laboratory mountain-top facility located in central New Mexico, USA (33.98° N, 107.18° W, 3.3 km altitude), using 3 separate radiometers. Fig. 2 shows the geometry of the observations, while Fig. 3 shows the instrument response and atmospheric transmission for each radiometer. The two photodiodes operating in the visible plus near-infrared (VNIR) range (Thorlabs model PDA100A) were pointed out of a glass window, as shown in Fig. 2a. The photodiodes operated in the 652–667 nm and 341–1098 nm bands, and hereafter they are simply referred to as the " H_{α} " and "VNIR" channels, respectively. The spectral responsivity of

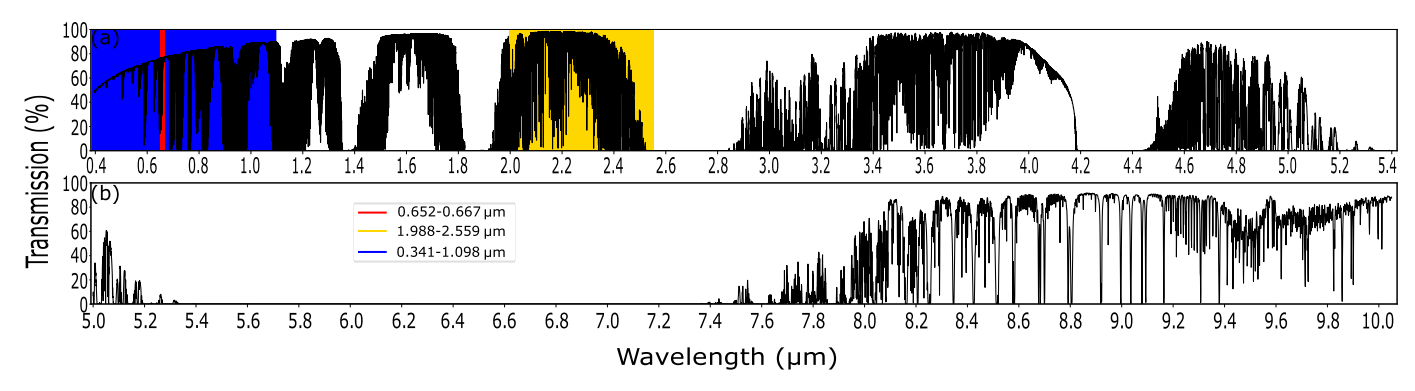


Fig. 1. Atmospheric transmission of visible and infrared light as a function of wavelength. Optical transmission was calculated through 10 km of atmosphere at the location and elevation of Langmuir Lab (3.3 km above mean sea level in central New Mexico) using MODTRAN (Berk et al., 2014). The 3 bands studied here are highlighted in blue, red, and yellow.

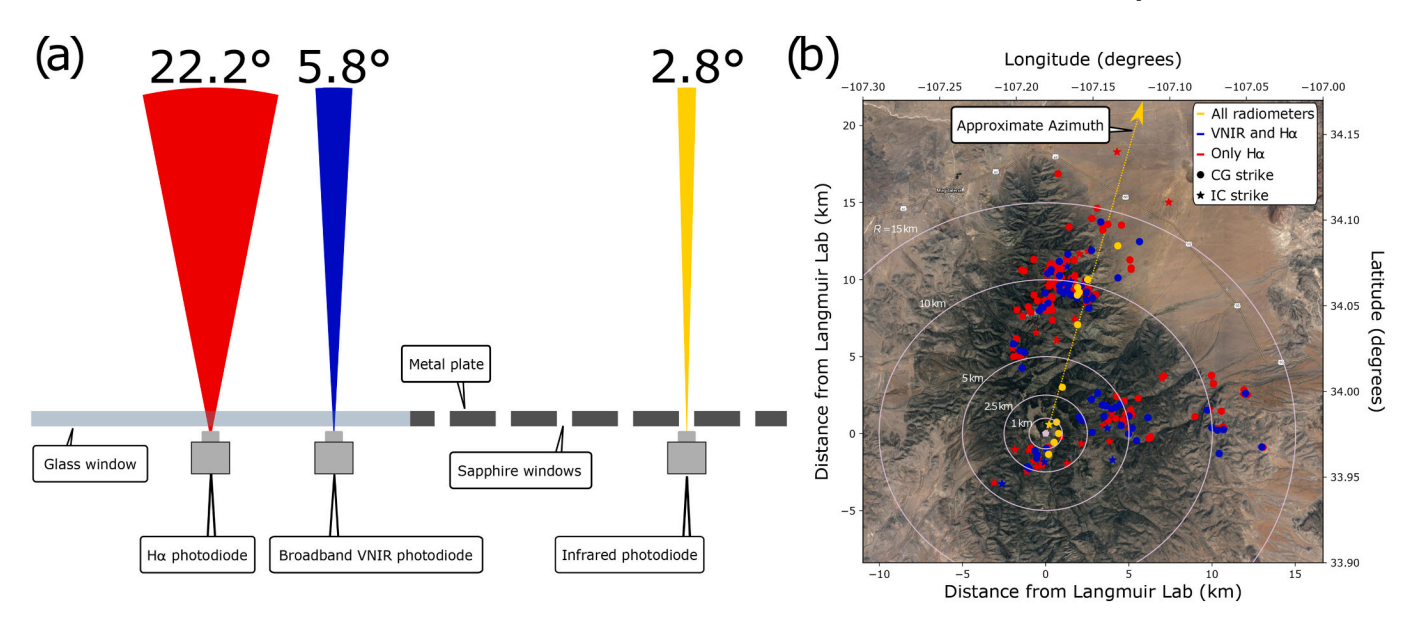


Fig. 2. (a) Equipment setup. The H_{α} and VNIR radiometers look through a glass window, while the infrared radiometer looks through a sapphire window. The field of view of each photodiode is shown to scale. (b) Lightning occurrence on August 10th, 2021 between 19:44 and 20:58 UTC. The pentagon at the center of the concentric circles represents the position of Langmuir Lab, while the concentric circles mark varying distances from the lab. IC flashes are represented by stars, while CGs are represented by circles. If data was captured by all three radiometers the symbol is colored yellow, if data was only captured by the H_{α} and VNIR radiometers it is colored blue, and if the data was only captured by the H_{α} radiometer then it is colored red. All of the positions are reported by ENTLN.

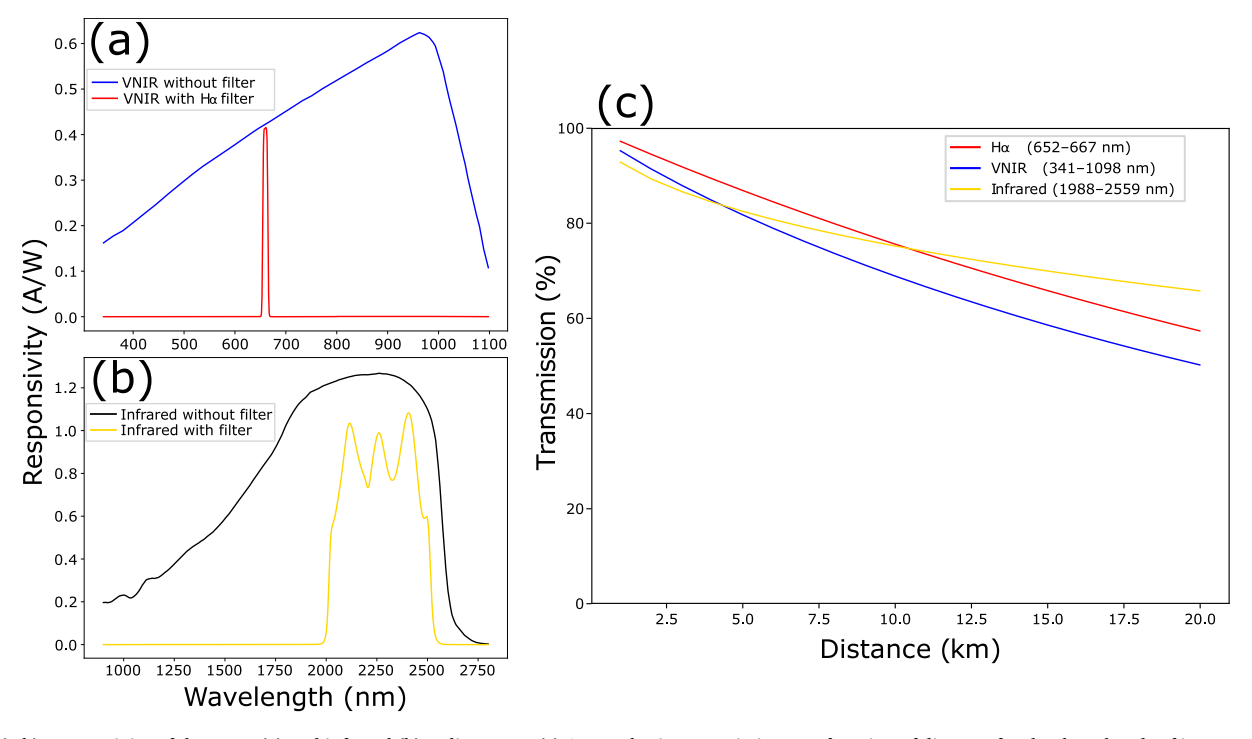


Fig. 3. (a-b) Responsivity of the VNIR (a) and infrared (b) radiometers. (c) Atmospheric transmission as a function of distance for the three bands of interest. The red (a) and yellow (b) traces show the combined effects of the detector response and filter used. The transmission, shown in panel (c), was obtained by convolving the detector response in panels (a) and (b) with the atmospheric transmission calculated with MODTRAN (Fig. 1) and and taking an average across the band of interest.

the H_{α} and VNIR photodiodes is shown in Fig. 3a. No filtering is done for the VNIR radiometer, and thus it also includes the near-infrared band up to 1 µm, similarly to what was done by Quick and Krider (2013) and Quick and Krider (2017). The H_{α} radiometer is built by including a 10 nm FWHM bandpass filter centered around 660 nm (Thorlabs FBH660-10). The H_{α} line appears to span ~50 nm in the spectrum collected by Walker and Christian (2017, Fig. 2), thus our radiometer may not collect all of the energy corresponding to this particular hydrogen transition.

Additionally, Walker and Christian (2017) show that there are two singly-ionized nitrogen lines very close to this band, which may also contribute to the total luminosity measured with our H_{α} radiometer.

The infrared radiometer was built using a Thorlabs PDA10DT photodiode and it is referred to simply as the "infrared" channel hereafter. Fig. 2a shows that, differently from the VNIR radiometers, it was pointed through a sapphire window that was set in a metal plate. The sapphire window allowed infrared radiation to transmit to the

photodiode across the entire range shown in Fig. 3b. Both glass and sapphire windows are about 2-mm thick. The Thorlabs PDA10DT photodiode detects radiation in the 1–2.6 μ m range. We limit the responsivity to the atmospheric transmission window of 1,988–2,559 nm with the aid of a filter. The resulting spectral responsivity is shown in Fig. 3b.

As shown in Fig. 2a, each radiometer had a unique field of view (FOV) dictated by the lens used to focus light onto the detector. Both the H_{α} radiometer and the broadband VNIR radiometer used an N-BK7 plano-convex lens while the infrared collection lens was a CaF₂ plano-convex lens. The H_{α} radiometer had the largest FOV (22.2°) due to the 25.4 mm focal length lens and 25.4 mm lens diameter, so it was used as the automatic trigger for the system. The broadband VNIR radiometer was the next largest with a focal length of 100 mm and lens diameter of 50.8 mm, which gave it a 5.8° FOV. Finally, the infrared radiometer had the smallest FOV (2.8°) due to its 12.7 mm lens diameter and 20 mm focal length. As demonstrated in Fig. 2b, the scattering of visible light allowed for the VNIR photodiodes to capture events outside of their field of view. Fig. 2b is described in detail in the Results section.

All data was collected with a Picoscope model 5442D and recorded to a local computer. This experiment was designed to run in an automated manner without an operator present during the observations. Once the H_{α} photodiode detected a nearby flash, the entire system triggered and 1 s of data was saved. The one-second interval was broken down into 200 ms of pre- and 800 ms of post-trigger data. The Picoscope traces were stored with 10 μ s temporal resolution (or 100 kHz sampling rate). This is much lower than the maximum bandwidth of the Picoscope (200 MHz). The sampling rate was roughly set as the minimal value required to capture the pulse waveshape within the bandwidth of the photodiodes, which were 2.4 MHz, 5.9 kHz, and 150 kHz, for the VNIR, H_{α} , and infrared photodiodes, respectively. Thus, the only radiometer that has a bandwidth lower than the sampling rate is the H_{α} . This happened due to the high gain setting chosen (70 dB). However, as it can be seen in Fig. 4, there is no significant loss of information when comparing the H_{α} traces with the detections of the other radiometers. The H_{α} trigger level was empirically determined to trigger off of nearby lightning return strokes, but in practice it also detected some IC flashes, as determined via comparison with Earth Networks Total Lightning Detection Network (ENTLN) data.

2.2. Alignment with ENTLN data

In order to measure source power in the VNIR and infrared bands, we need the approximate distance between source and observer. This distance was determined from lightning location data collected by ENTLN. Optical data was saved with local computer time information in the Picoscope software, accurate to the minute. To align the optical recordings with ENTLN's GPS time-stamped data, a comparison was performed for flashes with multiple strokes present in both data sets. Leveraging the fact that two interstroke intervals are rarely identical, the photodiode data could be matched to the ENTLN data, as shown in Fig. 4a.

Algorithmically, the alignment process was done by looking at all strikes that happened in the area within a minute of the radiometer data. Since the time difference between strikes should be preserved for both data collection systems, only the first strike in a flash had to be aligned to determine which strikes correlated with a peak in the photodiode data. The final decision was made by determining which alignment choice corresponded to the smallest time between other corresponding strikes, such as shown in Fig. 4a. This could be done for all flashes with multiple H_{α} peaks and strikes. An average (AVG) and standard deviation (STD) for the time offset were then calculated. Single-stroke flashes could be easily found by looking into the ENTLN data set an amount of AVG $\pm 2 \times$ STD seconds into the future. If a single ENTLN strike would be found in that window (which was normally the case), then we add the flash to the analysis, such as the example shown in Figs. 4c-d. This process yielded 53 flashes that could be analyzed with 193 CG strikes and 42 IC pulses. The Picoscope local time was on average 19.181 s ahead of the GPS time with a standard deviation of 296 ms.

After the alignment between the two data sets was completed, data for 235 optical pulses was augmented with the following information from ENTLN: peak current, polarity, type (IC versus CG), and distance. This technique can be easily employed to align other data sets (e.g., high-speed video, radio frequency recordings, etc.) with lightning location data.

2.3. Radiometer calibration

Each photodiode gives a voltage response that is dependent on the energy incident upon the diode and the respective gain setting. Therefore, to turn the photodiodes into radiometers they need to be calibrated. For the VNIR and H_{α} photodiodes this calibration was completed

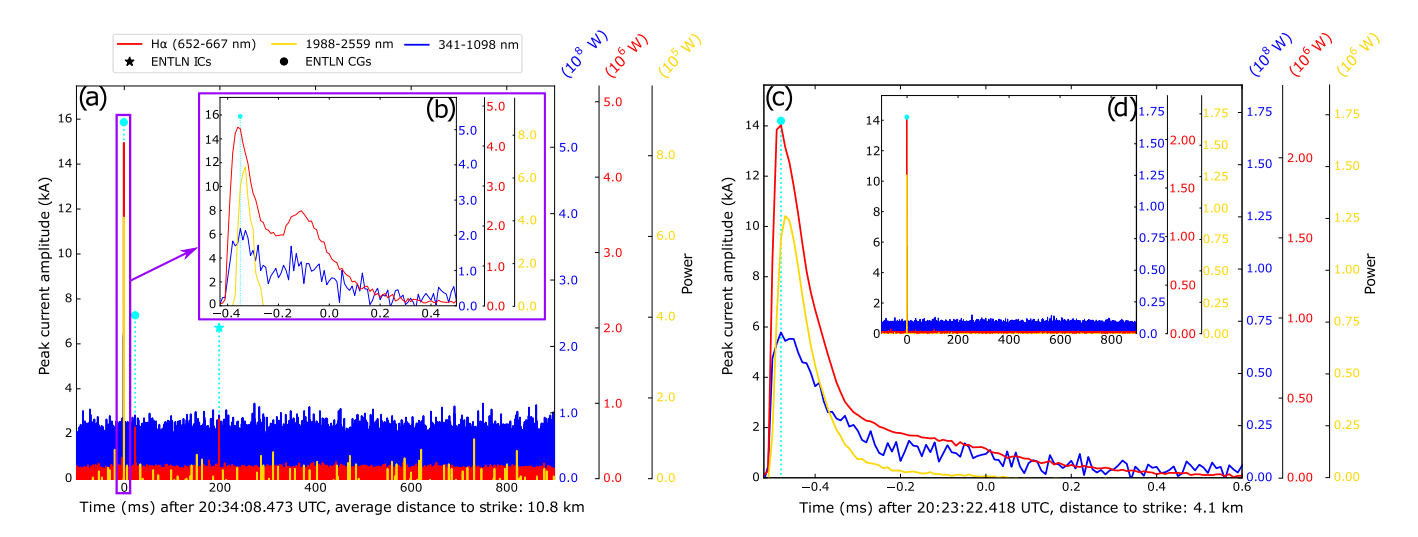


Fig. 4. Sample optical pulses detected for two cloud-to-ground flashes: (a–b) 20:34:08 UTC and (c–d) 20:23:22 UTC. Each panel shows the ENTLN peak current (in the left-hand side axis) and the optical power in the three channels (with three axis on the right-hand side) as a function of time. (a) Illustration of the alignment between optical pulses and ENTLN lightning location data. (b) Zoom into the first return stroke. (c–d) Panel (c) shows a zoom into the single-stroke flash shown in panel (d). All strikes shown in the figure are associated with negative source currents (cyan symbols).

with a 1,000 W Quartz Tungsten Halogen (QTH) lamp because it produces a specific known spectral irradiance 50 cm away from the source, as shown in Fig. 5a. The calibration is done by placing the QTH lamp at a known distance d away from the source and measuring the voltage yielded by the photodiode. A background measurement (with the lamp off) is also made and subtracted accordingly. The corresponding power at the aperture is determined by multiplying the spectral irradiance (in Fig. 5a) by any filters, integrating across the band of interest, scaling the power to the correct distance as $\propto (d/50 \text{ cm})^2$, and integrating over the aperture ($\pi D^2/4$), where D is the lens diameter. The lamp is moved to several different distances and the process is repeated. The resulting power at aperture for the VNIR photodiode versus measured voltage is shown in Fig. 5b.

In theory, the method for photodiode calibration is simple. However, the variable gain setting and the largely different intensities of lightning 10s of km away and a close-proximity lamp in the laboratory add a layer of complexity that may be challenging to deal with. Ideally, the calibration process would be done at the exact field-campaign gain settings and this was possible for the VNIR photodiode. However, the H_{α} photodiode's in-field gain setting was 70 dB and this was too sensitive to take calibration measurements with the QTH lamp in the laboratory. Additionally, the calibration method produces a linear fit to convert measured voltage to power at aperture, which best works if the calibration is done at similar voltages to those measured in the field.

Four different data collection strategies were employed in order to get calibration data with voltage levels similar to field records:

- collection with the same aperture and gain setting as used in the field campaign:
- 2. inclusion of a neutral density (ND) filter in front of the detector;
- 3. use of a smaller aperture (i.e., a lens with lower diameter);
- perform measurements at a lower gain setting than in the field (when applicable) and scale accordingly.

The effects of using strategies 1 through 3 can be seen in Fig. 5b–c for the VNIR radiometer. Technique number 4 does not apply in this case, because the photodiode was operated at 0 dB during the field campaign. The severe reduction in the spectral radiance produced by the ND filter can be seen in Fig. 5a. Thus, we can state that the detector is linear and properly calibrated in the range of interest. The same process is repeated for the H_{α} radiometer (not shown for the sake of brevity). The only difference is that we include measurements at lower gain than used in

the field (i.e., lower than 70 dB). The measured power scales with the gain setting (g in dB) as $\propto \! 10^{g/20}$. Similarly, an analogous process was used to calibrate the infrared photodiode. The only difference is that a blackbody-like source at different temperatures was used instead of the QTH lamp at varying distances. We would like to note that the responsivity charts in Fig. 3a and b show that the radiometers have no response outside of the desired band of operation. Thus, the measured infrared power is not a result of visible radiation leakage into the sensor.

The calibration process outlined above produces a linear relationship between voltage and observed optical power ($P_{\rm obs}$) at the detector in the band of interest in the form:

$$P_{\text{obs}}(t) = mV(t) + b,\tag{1}$$

where m and b are the slope and intercept calibration coefficients. Using the detected power at the photodiode and assuming a point source with isotropic emission, the source power can then be inferred according to Eq. (2) below:

$$P_{\text{source}}(t) = \frac{4\pi}{\Omega} \frac{P_{\text{obs}}(t)}{T(r)},\tag{2}$$

where T(r) is the transmission through the atmosphere as a function of distance from the radiometer to the return stroke, which was calculated with MODTRAN and is given in Fig. 3c for the three bands of interest (Berk et al., 2014). Notably, the background signal must be accounted for to get an accurate source power this was done by subtracting the median value of the entire record. In addition, $\Omega/4\pi$ is the fraction of the solid angle subtended by the detector, which is given as:

$$\frac{\Omega}{4\pi} = \sin^2 \left[\frac{1}{2} \arctan \left(\frac{D}{2r} \right) \right],\tag{3}$$

where D is the lens diameter and r is the distance to the strike. In the limit that $r\gg D$, Eq. (3) becomes the more familiar fraction between the detector area and the surface area of a sphere of radius r:

$$\frac{\Omega}{4\pi} = \frac{\pi (D/2)^2}{4\pi r^2}.\tag{4}$$

This method gives a calibrated radiometer response for each return stroke, such as the examples shown in Fig. 4. The energy was then determined with a numerical integral:

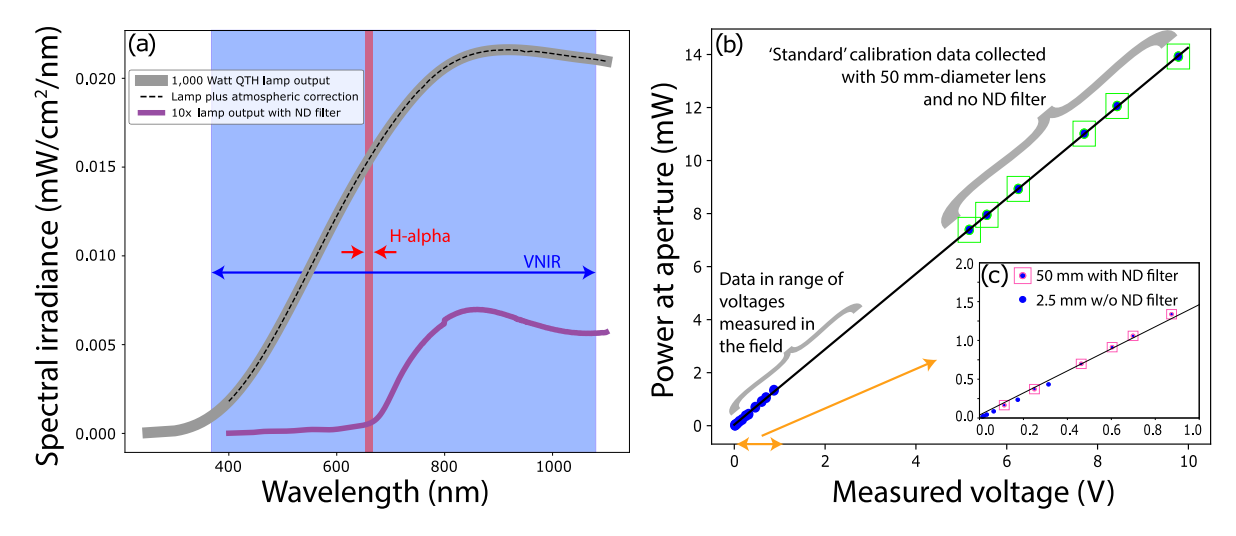


Fig. 5. (a) Spectral irradiance of the QTH lamp 50 cm away from the source (solid gray trace). The dashed line includes the (negligible) effect of atmospheric transmission through 50 cm of air, while the purple trace shows the effect of the ND filter (the trace is amplified $10 \times$ to aid the visualization). (b) Calibration data for the VNIR radiometer. (c) A zoom into the 0–1 V range discriminating the data collection performed with alternative techniques to probe the instrument's linear trend at low voltages. In the legend of panel (c), 50 and 2.5 mm stand for the lens diameter used.

$$E_{\text{source}} = \int_{t_{\text{num}}}^{t_{\text{end}}} P_{\text{source}}(t) dt, \tag{5}$$

Where $t_{\rm start}$ and $t_{\rm end}$ are the pulse start and end times, respectively, determined by when the source power first and last exceeds 10% of its peak value (i.e., on either side of the pulse). In the Results section we report values for the peak of $P_{\rm source}$, the integrated $E_{\rm source}$, and the pulse duration, given as $t_{\rm end} - t_{\rm start}$. Please note that Eq. (2) does not include any effects of cloud scattering between source and observer. Potential effects of cloud scattering in the measurements are discussed in Section 4.1.

3. Results

We detected 527 light pulses on August 10, 2021 within 19 km of Langmuir Lab with our H_a radiometer. These pulses are distributed over 53 different one-second triggers in our radiometer system. Among the 527 optical pulses, 235 of them were correlated with natural lightning strikes in a small convective cell, as detected by ENTLN, using the methodology outlined in Section 2.2. We focus the analysis on these 235 strikes for which both radiometry and lightning location data are available, because otherwise we cannot estimate source power according to Eq. (2). The data in Fig. 2b is a visualization of that afternoon's storm, and it differentiates between CG and IC strikes by representing them with circles and stars, respectively. There are 139 red data points and they indicate that only the H_{α} radiometer captured the pulse in those cases. There are 72 blue data points and they indicate that both the H_{α} and the VNIR radiometer saw the pulse. Finally, there are 12 yellow data points which indicate that all three radiometers collected data for that optical pulse. The pentagon is the position of Langmuir Lab and the same-colored concentric circles mark specific distances away from the lab. This figure displays a lack of spread in the infrared data which implies that the main contributor to the lack of infrared measurements was the narrow 2.8° field of view set by the lens. While both of the other radiometers had a limiting field of view, the scattering of visible light allowed the VNIR and H_{α} radiometers to catch many strikes outside of the field of view. The lightning strikes recorded behind Langmuir Lab were due to the south-facing windows that let the light from strikes happening behind the radiometers get through and reflect off the metal plate shown in Fig. 2a.

Fig. 4 shows two different sample flashes; the red-colored curve is calibrated optical power in the H_{α} band, the blue-colored curve is calibrated optical power in the VNIR band, and the yellow curve is calibrated optical power in the infrared band. Notably, the order of magnitudes of the power axes (on the right) decreases from left to right. Fig. 4a demonstrates the alignment process discussed in Section 2.2, while Fig. 4b is a zoomed-in portion of the triggering return stroke. Fig. 4b shows that this particular return stroke is followed by an Mcomponent. The M-component is the second luminosity bump seen in the visible and H_{α} channels, but interestingly, not in the infrared. The second sample flash, shown in Fig. 4c and d, had a single return stroke. This particular return stroke had a time difference from ENTLN data that was 1.35 standard deviations above the average time delay (18.9 s ahead of ENTLN time). All of the samples demonstrate that the H_{α} radiometer, which has the most sensitive gain setting, was the most reliable source of data acquired in the campaign. This figure also demonstrates the effects of the low-gain setting on the broadband VNIR and infrared photodiodes. All apparent pulses seen in these two channels in Fig. 4a after 300 ms are at the noise level.

Fig. 6 shows the measured optical properties as a function of peak current in the H_α , broadband VNIR, and infrared radiometers in the top,

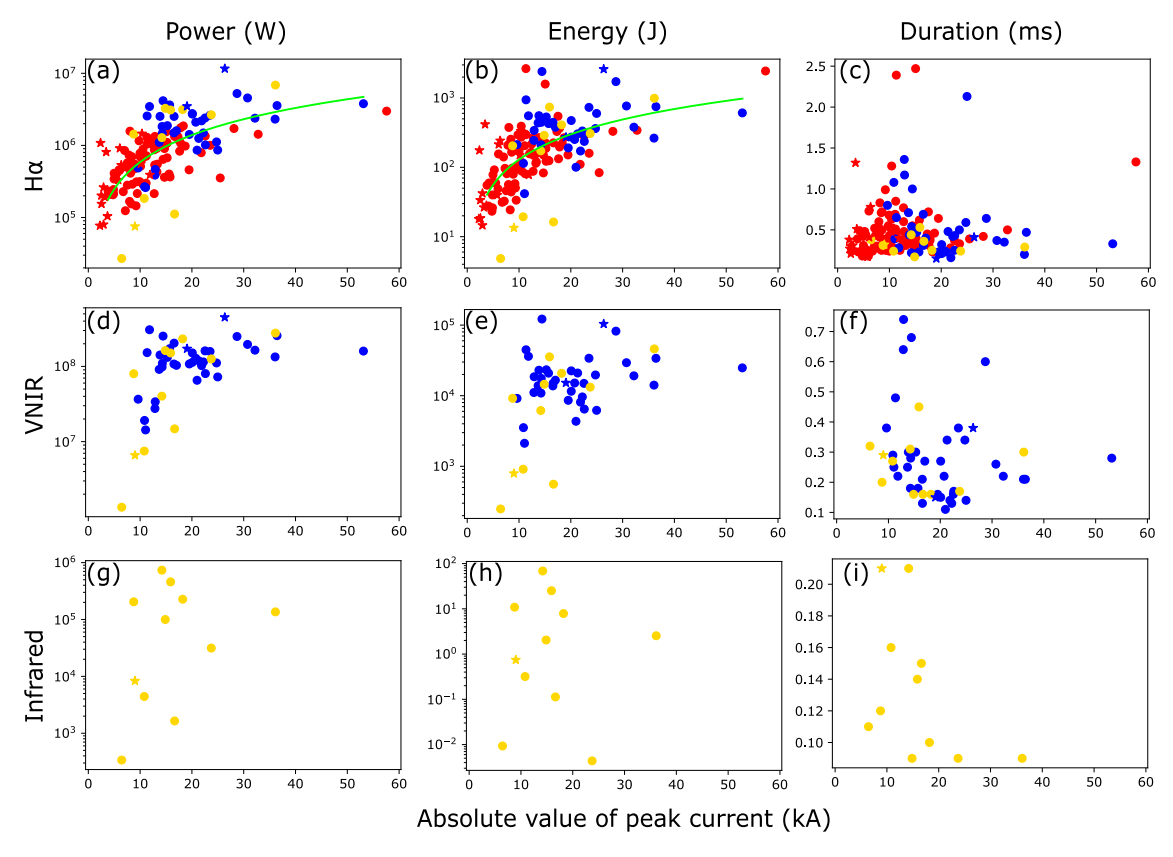


Fig. 6. Key properties of optical pulses as a function of peak current: peak radiated power (a,d,g), total radiated energy (b,e,h), and duration (c,f,i), in the H_a (a–c), VNIR (d–f), and infrared (g–i) channels. The figure contains only flashes generally within the field of view. If data was captured by all three radiometers the symbol is colored yellow, if data was only captured by the H_a and VNIR radiometers it is colored blue, and if the data was only captured by the H_a radiometer then it is colored red. The circles represent CGs, while the stars represent ICs. For instance, a yellow circle in the top row indicates that the data point corresponds to a CG strike detected in all three channels.

middle, and bottom rows, respectively. The figure uses the same color scheme and CG/IC labeling method as Fig. 2b, but it only includes flashes in the field of view. The columns from left to right display the calibrated source power measured in Watts (W), the calibrated source energy measured in Joules (J), and duration of each stroke in milliseconds (ms). It can be seen that emitted power and energy generally increase with peak current, but there is considerable scattering along the trend. The same cannot be said about the optical pulse duration. Much like one could expect, the radiation scattering in the cloud makes IC pulses fundamentally different in magnitude and duration from the CG ones. While IC pulses do blend inside of the range of amplitudes and durations reported for CG pulses, they are primarily found in the lowpeak current sections of all graphs in Fig. 6. The durations reported in Fig. 6c are the best measure of the optical pulse duration we have, since the H_{α} radiometer had the most sensitive gain setting. The average duration of optical pulses for negative -CG flashes within the field of view is 0.49 ± 0.36 ms, which is somewhat consistent to the findings of Quick and Krider (2013), despite the fact they use a different method to determine the pulse duration. There were only 3 of these CGs that lasted longer than 2 ms. All of them were followed by large M-components, such as the one shown in Fig. 4b. There is a single IC event that produced measurable infrared radiation but it occurred less than 1 km away from the observation facility and directly in front of the field of view. There were no other IC events that produced infrared radiation. There are 2 +CGs in the data set, but one was 17 km away from the observation site, while the other was the furthest east pulse seen on 33.988° N latitude. Thus, both +CG flashes were only seen in the H_{α} channel.

Table 1 summarizes the average properties of the entire data set. In this paragraph, we will focus on -CGs that are generally within the field of view, i.e., Section (c) of the table. Negative CGs have an average peak current of -14.5 ± 7.8 kA. These strikes had peak power of 130 ± 74 MW and total emitted energy of 20 ± 21 MJ in the VNIR range. Additionally, -CGs had peak radiated powers of 1.2 ± 1.1 MW and 0.19 ± 0.23 MW in the H_{α} and infrared bands, respectively. The total radiated energy in these two bands is 290 ± 380 J and 12 ± 20 J, respectively. In addition to the data shown in Fig. 6, the table gives average power ratios for each channel with respect to the VNIR band. This information gives a novel quantification that the ratio between the power emitted in the 2–2.5 μm infrared and VNIR bands is 2.7×10^{-3} . This value is discussed in Section 4.2 below. In addition, the H_{α} peak power amounted to 1.7% of the VNIR peak. Our estimates of the average return stroke power radiated in the VNIR band yields values that are two orders of magnitude lower than the findings of Quick and Krider (2013). Possible reasons for the discrepancy are given in Section 4.1 below. The median error in power estimates due to lightning location uncertainty are 15, 14, and 23%, for the VNIR, H_{α} , and infrared bands, respectively.

Comparing the three different sections in Table 1, we can see that neither IC flashes (a), or CG flashes outside of the field of view (b) affect the average properties significantly. The largest difference between parameters in the three sections of the table is 30%. It can also be seen that the standard deviation is often greater than the average for several parameters reported on the table. This happens because these parameters are not distributed normally as a function of peak current. Instead of Gaussian, their distribution is (roughly) Exponential. For an (exact) Exponential distribution, the average and standard deviation are identical.

Fig. 6a and b display an attempt to fit a trend line to the measured peak power and energy. The attempt includes -CGs only to reduce uncertainty and to allow for comparison with Quick and Krider's results. The green trend line has the form $y = Kx^p$, where K and p are fit constants. For the radiated power, the power-law exponent was found to be p=1.25, while for the energy it was 1.21. These p values indicate that the trend line lies in between a linear and a quadratic relationship. This is roughly consistent with the findings of Quick and Krider (2013, Fig. 12), who reported that linear and quadratic functions fit the relationship between peak power and peak current with similar R^2 values. The trend line was only determined for the H_{α} radiometer because the broadband VNIR radiometer's gain was not set high enough to pick up any of the low current/low power events, in addition, the infrared radiometer only had 11 CG strikes. The R² value for the fit in Fig. 6a and b is 0.36 and 0.46, respectively. The trend lines obtained by fitting the H_{α} channel data can be expected to apply to the VNIR values as well, since they are linearly proportional to each other. A plot of the H_{α} versus VNIR power (not shown) displays a linear relationship between them with a zero intercept and $R^2 = 0.92$. The same cannot be said for the infrared channel.

da Silva et al. (2019) showed that the delay between current and optical emissions in rocket-triggered lightning is attributed to the plasma nature of the lightning channel resistance. Particularly, they showed that the finite time it takes to heat the plasma (da Silva and Pasko, 2013) to ~30,000 K results in a delay of ~0.1 μ s between the surge of current and optical emissions. The data set presented here creates the opportunity to discuss the relationship between peak radiated power and peak current, which follows a power-law dependence $P \propto I^p$, with p being a number between 1 and 2. This behavior can be understood as follows. The instantaneous electrical power per unit channel length available to excite optical emissions is RI^2 , where R is the channel resistance per unit length and I is the current. One can expect that a fraction η is emitted as optical power in the band of interest (e.g., around the H_α line). Without further inspection, this expression would indicate that the radiated power is $P = \eta RI^2 \propto I^2$, in alignment with the

Table 1

Optical properties measured with radiometers in three different bands. Section (a) includes data from CGs and ICs of both polarities, while section (b) shows results exclusively for –CGs. Section (c) narrows the results further to include only –CGs in the field-of-view. Quantities are given as a mean plus or minus standard deviation. The last column shows the ratio of the power measured by that instrument to the power measured by the broadband VNIR radiometer.

| Peak Current (kA) | | Number | Power (W) | Energy (J) | Duration (ms) | Power Ratio |
|-------------------|-----------------|--------|------------------------|-----------------------|-----------------|------------------------------|
| (a) Entire dat | a set | | | | | |
| H_{α} | | 235 | $1.0\pm1.3\times10^6$ | $2.8\pm4.3\times10^2$ | 0.56 ± 0.40 | $1.7 \pm 0.5 	imes 10^{-2}$ |
| VNIR | 14.7 ± 10.3 | 84 | $1.0\pm0.91\times10^8$ | $1.9\pm2.3\times10^4$ | 0.33 ± 0.19 | 1 |
| Infrared | | 12 | $1.6\pm2.2\times10^5$ | 9.5 ± 19 | 0.13 ± 0.04 | $2.4 \pm 4.9 \times 10^{-3}$ |
| (b) –CGs only | y | | | | | |
| H_{α} | | 193 | $1.1\pm1.1\times10^6$ | $2.9\pm4.0\times10^2$ | 0.55 ± 0.41 | $1.7 \pm 0.5 	imes 10^{-2}$ |
| VNIR | 15.6 ± 9.5 | 75 | $1.1\pm0.83\times10^8$ | $1.9\pm2.2\times10^4$ | 0.32 ± 0.19 | 1 |
| Infrared | | 11 | $1.7\pm2.2\times10^5$ | 11 ± 20 | 0.13 ± 0.04 | $2.5 \pm 5.1 \times 10^{-3}$ |
| (c) –CGs in F | OV only | | | | | |
| H_{α} | | 130 | $1.2\pm1.1\times10^6$ | $2.9\pm3.8\times10^2$ | 0.49 ± 0.36 | $1.7 \pm 0.5 	imes 10^{-2}$ |
| VNIR | 14.5 ± 7.8 | 46 | $1.3\pm0.74\times10^8$ | $2.0\pm2.1\times10^4$ | 0.28 ± 0.15 | 1 |
| Infrared | | 10 | $1.9\pm2.3\times10^5$ | 12 ± 20 | 0.13 ± 0.04 | $2.7 \pm 5.3 \times 10^{-3}$ |

experimental findings of Zhou et al. (2014). However, the lightning plasma exhibits a negative differential resistance, which has the form: $R=A/I^b$, where A and b are positive constants. da Silva et al. (2019, Table 1) showed that in a range of scenarios b is of the order of 1. As a conclusion, the radiated power should scale as $P \propto I^{2-b}$, where the power-law exponent (2-b) is by definition a number lower than 2. Carvalho et al. (2015) determined that in rocket-triggered lightning flashes this trend is $P \propto I^{1.75}$, while our data set suggests that it is $\propto I^{1.25}$. In summary, the reason for the power-law exponent being lower than 2 is the the plasma's negative differential resistance behavior.

Liu et al. (2021) found that the 337-nm peak brightness of Narrow Bipolar Events (NBEs) near cloud tops increases linearly with peak current. The optical brightness was detected by ASIM, while the peak current was provided by Vaisala's GLD360 lightning detection network. This result is somewhat similar to what we found here despite the fact that NBEs are produced by streamer corona discharges (Attanasio et al., 2019; Attanasio et al., 2021; Rison et al., 2016). There is no reason for why streamer corona discharges and return strokes should exhibit such a similar trend, since their emission mechanisms are vastly different. The former consists of a non-equilibrium plasma with high electron temperatures, but near-ambient neutral gas temperatures. The latter is a hot plasma in thermodynamic equilibrium. This newfound similarity is highlighted as an important topic for future investigation.

4. Discussion

4.1. Reasons for the low power detected in the VNIR band

The main goal of lightning radiometry is to provide calibrated measurements of the lightning channel's optical output. We dedicated a substantial amount of work to ensure that the calibration was done correctly, as discussed in Section 2.3. Despite our diligent efforts, which included repeating the calibration process several times with different: methods, engineers, and (duplicate) photodiodes, our estimates on peak optical power emitted in the VNIR band differ from the results obtained by Quick and Krider (2013) in Arizona by two orders of magnitude, with ours being lower. Our values are closer to, but still a factor of 4 lower than, the figures reported by Guo and Krider (1982) in Florida. Several potential reasons for this discrepancy are discussed below.

- 1. Low sampling rate. Walker and Christian (2017); Walker and Christian, 2019 showed that the lightning spectrum changes substantially in the microsecond time scale. Quick and Krider (2017) showed that, for rocket triggered lightning, the optical emission for a channel section near the ground has a strong surge that lasts roughly 20 μ s followed by a longer period of weaker luminosity. Our sampling rate of 100 kHz may not be sufficient to capture the actual peak of optical power. Quick and Krider (2017) used a 10 MHz data acquisition system.
- 2. Non-uniform spectral response of the photodiode. Carvalho et al. (2018) showed that photodiodes with different spectral response in the VNIR range produce optical pulse waveshapes that can be vastly different. Fig. 3a shows the spectral response of the Thorlabs PDA100A photodiode used in this investigation. It can be seen that it has a distinct peak within the near-infrared range, just below 1 µm. On the other hand, the photodiode used by Quick and Krider (2013) has an approximately flat spectral response within the VNIR band. For this reason alone a straight comparison between the two measurements may not be feasible.
- 3. Spectral irradiance of lightning versus the calibration lamp. There is no reason to believe that the spectrum of the QTH lamp used here for calibration (Fig. 5a) is identical to the spectrum of a lightning flash. Actually, comparison with lightning spectra available in the literature shows a reverse trend than the one displayed in Fig. 5a. Lightning spectral irradiance decays with increasing wavelength due to

the fact that continuum radiation peaks in the visible and has a much lower contribution in the infrared (Uman, 1963; Orville and Uman, 1965; Orville and Henderson, 1984; Weidman et al., 1989). It is unclear what is the spectral irradiance of the calibration lamp used by Quick and Krider (2013). In combination, items #2 and #3 suggest that our VNIR radiometer is more sensitive to the near-infrared portion of the optical spectrum, instead of the visible. Thus, it is quite natural that our inferred source power is lower than what was estimated by Quick and Krider (2013).

- 4. Data is biased by sources outside of the field of view. In this investigation, we introduce an automated system to detect the optical power radiated by lightning, which of course has its caveats. A simple explanation for the low power detected is that the average value is biased by strikes outside of the field of view (FOV). The analysis shown in Table 1 indicates that this is not the case. The average power in the VNIR band for the entire data set, —CGs only, and —CGs in FOV only, reported in Sections (a), (b), and (c) of the table, respectively, differs by no more than 30%. It is possible, however, that the narrow FOV consistently detected only a portion of the return stroke channel.
- 5. *Cloud scattering.* Another plausible explanation is that the lightning discharge is obscured by clouds in between the source and observation site. Langmuir Lab is a mountain-top facility located at 3.3 km altitude and, as a result, orographic effects favor condensation and convection around the lab. Fig. 7 illustrates the potential effects of cloud scattering using the methods provided by Koshak et al. (1994) and Luque et al. (2020). First, Fig. 7a shows the photon flux exiting a cloud for sources placed at three different depths. These curves correspond to a solution to the photon diffusion equation, given in closed form in Eq. (27) of Luque et al. (2020). We use a diffusion coefficient of 10 km²/ms, corresponding solely to Mie scattering of visible photons by cloud hydrometeors (no absorption is included). Second, we convolve the photon flux with a 20-µs-wide optical pulse (see justification in item #1 above). Fig. 7b shows that the presence of clouds in between source and observer reduces the amplitude and widens the detected optical pulse. In this particular case, a cloud depth of 1.9 km explains how a 20-µs pulse can appear as wide as 0.14 ms in the detector (see also Soler et al., 2020, Eq. (1) and related discussion). The VNIR pulse shown in Fig. 4c is reproduced in Fig. 7b for comparison. At the same time that the pulse widens by a factor of 7, its amplitude is reduced by a factor of 14. Stronger attenuation can be produced by larger cloud depths. The 4-km depth example included in Fig. 7b produces attenuation by a factor of 57. However, this comes at the expense of widening the optical pulse even further.

The objective of this discussion section is to emphasize that calibrated measurements of the lightning optical power are quite challenging. Particularly, that the inferred absolute source power can be affected by all issues discussed above. These issues may be related to the observation conditions, experimental setup, and/or detector calibration. All of which can be different for data sets collected by different research groups, which makes comparisons between published research on the topic challenging. There still is a long road ahead of the atmospheric electricity research community before we can make radiometric measurements part of the observational routine in lightning observatories across the globe. Some examples of instruments used by lightning researchers, which make 'standard' measurements, and allow for data set comparisons across the globe are lightning location systems and high-speed cameras. We hope with this article to outline the issues that need to be addressed in order to make radiometers a routine instrument.

4.2. Fraction of power emitted in the 2–2.5 μ m infrared band

The ratio between optical power emitted in the H_{α} and VNIR bands, equal to 1.7%, seems quite reasonable. The fraction is roughly identical to the ratio between the band widths, which is 1.9%. However, the same

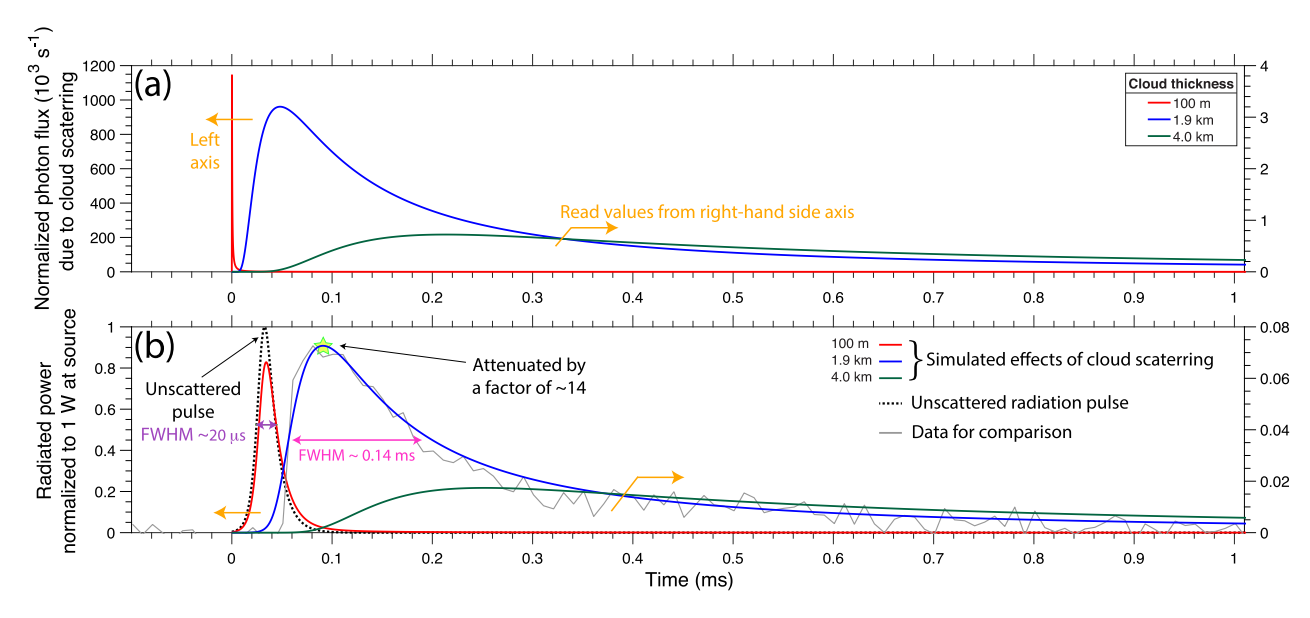


Fig. 7. (a) Photon flux exiting clouds of different depths (100 m, 1.9 km, and 4 km). The flux is normalized per unit source photon (Luque et al., 2020, Eq. (27)). (b) A 20-μs optical pulse (black dashed trace) is convolved with the flux in (a) to simulate the effects of cloud scattering (red, blue, and green traces), and compared to data (gray trace). Values for the black and red curves should be read from the left-hand side axis, while values for all other curves should be read from the right.

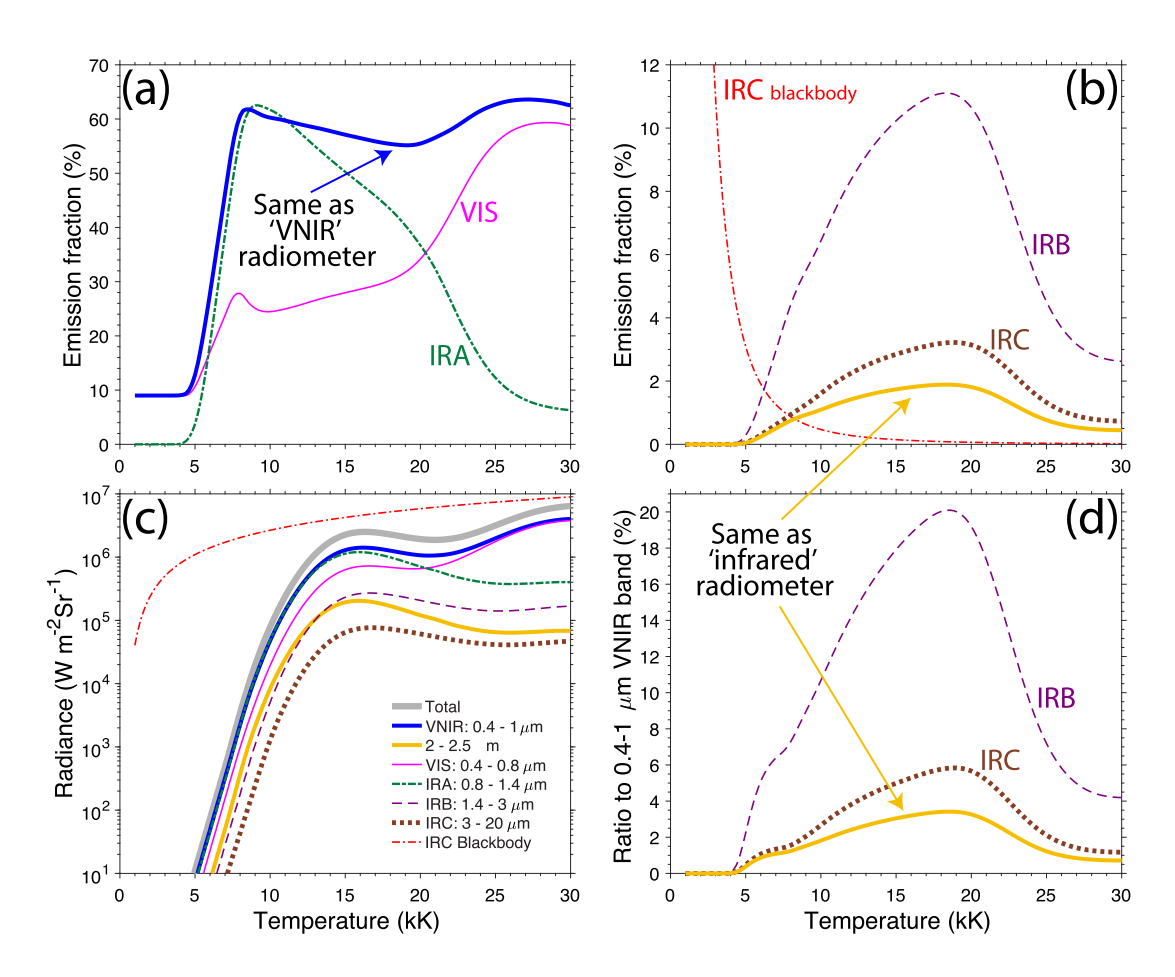


Fig. 8. (a-b) Fraction of radiance in selected bands of the optical spectrum. (c) Total radiance and breakdown in selected bands of interest. (d) Estimated ratio of power radiated in selected bands to the power emitted in the VNIR band (0.4–1 µm). All panels are given as a function of temperature. The total radiance of an air plasma, and the contributions of the visible (VIS) and infrared (IRA, IRB, and IRC) bands shown in panel (c) were obtained from Cressault et al. (2015).

rationale does not apply for the comparison between power emitted in the VNIR and 2–2.5 µm infrared bands, since the lightning spectra can be expected to be quite different in these two regions. In order to put our findings into perspective, we look into the radiance of an air plasma at local thermodynamic equilibrium (LTE) calculated by Cressault et al. (2015). Fig. 8 shows these authors' calculations up to 30,000 K for several different bands of the optical spectrum, including the visible $(0.4-0.8 \mu m, VIS in the figure)$ and the three infrared bands: IRA (0.8-1 μ m), IRB (1.4–3 μ m), and IRC (3–20 μ m). The IRC band extends all the way to 1,000 μm, but there is virtually no plasma emission beyond 20 μm (Cressault et al., 2015). Fig. 8a and b show the fraction of radiance in selected bands of interest, which are calculated by taking the ratio between a band-specific radiance and the total one, as shown in Fig. 8c. Cressault et al. (2015) do not report the radiance in the precise bands of interest for our analysis, 0.4-1 and 2-2.5 μm , thus they need to be estimated. According to the measurements made by Laux et al. (1995), 58% of the energy radiated by an air plasma at 8,000 K in the IRA band comes from the near-infrared range (0.8–1 μ m). Therefore the fraction of optical power emitted in the range of our broadband VNIR radiometer can be estimated as $\eta_{\rm VNIR}=\eta_{\rm VIS}\,+0.58\eta_{\rm IRA}$, where $\eta_{\rm VIS}$ and $\eta_{\rm IRA}$ are the fraction of optical power radiated in the visible and infrared A bands, respectively, as shown in Fig. 8a. Similarly, from the work of Laux et al. (1995), one can infer that 17% of the energy emitted in the IRB band lies within the 2-2.5 µm range. Therefore, the fraction of optical power emitted in the band measured by our 'infrared' radiometer is given as $\eta_{\rm 2-2.5\,\mu m} = 0.17 \eta_{\rm IRB}.$ These two fractions are displayed in Fig. 8a and b, respectively.

We proceed to estimate the ratio between the power emitted in the bands of our infrared and VNIR detectors as $\eta_{2-2.5\,\mu\mathrm{m}}/\eta_{\mathrm{VNIR}}$. The resulting fraction is shown in Fig. 8d (yellow trace) alongside similar estimates for the IRB and IRC bands. In the temperature range of a cooling return stroke channel, 10,000–20,000 K, the ratio is $\sim 2 \times 10^{-2}$, and it is lower for higher temperatures. The value inferred from the measurements, 2.7×10^{-3} , is only a factor of 7 lower than this figure, so we deem the agreement reasonable. Nonetheless, there are two probable reasons for the discrepancy. Firstly, the field of view of the infrared radiometer was quite narrow, only 2.8°, which can cover a 500-m wide object located 10 km away from the lens. This may not be sufficient to cover the entire flash and its branches between cloud and ground. The field of view of the broadband VNIR radiometer is twice as large, and can fully see a target that is 1-km wide at a distance of 10 km. Secondly, IC and CG strikes of similar current seem to emit similar powers in the VNIR band. This indicates that, potentially, a large portion of the VNIR energy seen from the ground comes from cloud illumination (Section 4.1), i.e., from the portion of channels that are inside of the cloud. Visible and near-infrared radiation have difficulty escaping clouds — a photon is scattered several times before it may be able to escape. But a good portion of the VNIR energy does escape. This is the mechanism which makes lightning mapping from Geostationary orbit possible (Goodman et al., 2013). However, lightning channels inside the cloud may emit a lower proportion of its energy in infrared and cloud scattering may affect the propagation of infrared radiation differently than visible. All these reasons may explain why the observed ratio between power detected by our infrared and VNIR radiometers is lower than the theory predicts. But further research is required to clarify this issue.

For the sake of discussion, we have included in Fig. 8b the fraction of optical power radiated by a blackbody in the IRC band, as given by Siegel (2001, pages 20-22). It can be seen that an air plasma does not behave as a blackbody at all. While the fraction of energy radiated in the IRC band is lower than an LTE air plasma, the total radiance in this band is substantially overestimated, as shown in Fig. 8c. The blackbody radiance in this band is actually larger than the total radiance of an air plasma. The conclusion here is that Planck's law for the radiance of a blackbody must not be used in a direct way to infer the temperature of lightning. But nonetheless, for a blackbody, the fraction between the

radiance in the 2–2.5 µm to the one in the 0.4–1 µm band is $\sim 9\times 10^{-3}$ for temperatures in the range between 10,000 and 20,000 K, which is still 3 times larger than the 2.7×10^{-3} figure derived from the measurements.

Finally, another important discussion point is that the trends shown in Fig. 8 agree qualitatively with independent calculations by Pérez-Invernón et al. (2022). The VIS and VNIR radiances in Fig. 8c increase with plasma temperature in agreement with the 380–780 nm calculations of source power emitted per unit channel length by Pérez-Invernón et al. (2022), shown in their Fig. 7. Furthermore, the IRA and 2–2.5 μ s radiances peak in the 10,000–20,000 K range and decrease for higher temperatures above 20,000 K. This is in qualitative agreement with the estimates of power output around the 777.4 nm oxygen line by Pérez-Invernón et al. (2022). As speculated in the Introduction, both of these data sets support the idea that observations in infrared bands may provide unique insights into processes that take place at temperatures lower than the return stroke channel, such as leaders, for example.

5. Conclusions

In this work, we have reported radiometric observations of lightning in the visible and infrared ranges. More specifically, we report peak radiated power and total radiated energy in the VNIR range (0.4–1 μm), around the H_{α} line (652–667 nm), and for the 2–2.5 μm infrared band. The estimated peak power and total energy radiated by –CGs in the VNIR range is 130 MW and 20 kJ, respectively. Additionally, our measurements indicate that the ratio between the power emitted in the H_{α} and 2–2.5 μm bands to the VNIR are 1.7×10^{-2} and 2.7×10^{-3} , respectively. The relationship between optical emission around the H_{α} line and peak return stroke current follows a power law, with the exponent ranging between 1.25 for peak power to 1.21 for total energy, and this trend should be true across the entire visible spectrum. This power-law relationship is attributed to the plasma negative differential resistance of lightning channels.

This work is a first step towards extending lightning radiometry to other bands of the optical spectrum beyond the visible range. We have encountered and analyzed the challenges in measuring optical power in the visible and infrared regimes. Differences in observation conditions, experimental setup, and calibration methods make it impractical to compare our results to what has been previously reported in the literature. This helps emphasize that there still is a long road ahead of our research community to make multi-band calibrated radiometric measurements of lightning optical power and routinely monitor its plasma properties.

CRediT authorship contribution statement

Jacob Wemhoner: Conceptualization, Methodology, Software, Validation, Formal analysis, Investigation, Data curation, Visualization, Writing - original draft, Writing - review & editing. Lydia Wermer: Conceptualization, Methodology, Software, Validation, Formal analysis, Investigation, Resources, Data curation, Supervision, Project administration, Funding acquisition, Writing - original draft, Writing - review & editing. Caitano L. da Silva: Conceptualization, Methodology, Validation, Formal analysis, Investigation, Resources, Data curation, Visualization, Supervision, Project administration, Funding acquisition, Writing - original draft, Writing - review & editing. Patrick Barnett: Conceptualization, Methodology, Software, Validation, Formal analysis, Investigation, Resources, Writing - review & editing. Cameron Radosevich: Conceptualization, Methodology, Software, Validation, Formal analysis, Investigation, Resources, Writing - review & editing. Sonal Patel: Methodology, Software, Validation, Formal analysis, Investigation, Resources, Writing - review & editing. Harald Edens: Investigation, Resources, Supervision, Project administration, Funding acquisition, Writing - review & editing.

Declaration of Competing Interest

The authors declare no competing interests.

Data availability

Radiometric data used in this publication is available at https://zenodo.org/record/7693798/#.ZAJqZ-zMLUJ. ENTLN data can be obtained freely by request from Earth Networks (https://www.earthnetworks.com).

Acknowledgments

This research has been supported by the Laboratory Directed Research and Development program at Sandia National Laboratories, a multimission laboratory managed and operated by National Technology and Engineering Solutions of Sandia LLC, a wholly owned subsidiary of Honeywell International Inc. for the U.S. Department of Energy's National Nuclear Security Administration under contract DE-NA0003525. The research at New Mexico Tech has also been supported by NSF CAREER award AGS-2046043. We thank Earth Networks for providing ENTLN lightning location data. We also thank Prof. K. Minschwaner for insightful discussions on basic radiometry principles.

This article has been authored by an employee of National Technology & Engineering Solutions of Sandia, LLC under Contract No. DE-NA0003525 with the U.S. Department of Energy (DOE). The employee owns all right, title and interest in and to the article and is solely responsible for its contents. The United States Government retains and the publisher, by accepting the article for publication, acknowledges that the United States Government retains a non-exclusive, paid-up, irrevocable, world-wide license to publish or reproduce the published form of this article or allow others to do so, for United States Government purposes. The DOE will provide public access to these results of federally sponsored research in accordance with the DOE Public Access Plan https://www.energy.gov/downloads/doe-public-access-plan.

References

- Attanasio, A., Krehbiel, P.R., da Silva, C.L., 2019. Griffiths and Phelps lightning initiation model, revisited. J. Geophys. Res. 124, 8076–8094. https://doi.org/10.1029/2019.ID030399.
- Attanasio, A., da Silva, C.L., Krehbiel, P.R., 2021. Electrostatic conditions that produce fast breakdown in thunderstorms. J. Geophys. Res. Atmos. 126, e2021JD034829 https://doi.org/10.1029/2021JD034829.
- Berk, A., Conforti, P., Kennett, R., Perkins, T., Hawes, F., van den Bosch, J., 2014.
 MODTRANG: a major upgrade of the MODTRAN radiative transfer code. In: Velez-Reyes, M., Kruse, F.A. (Eds.), Algorithms and Technologies for Multispectral,
 Hyperspectral, and Ultraspectral Imagery XX. International Society for Optics and Photonics. SPIE, pp. 113–119. https://doi.org/10.1117/12.2050433.
- Boggs, L.D., Liu, N., Nag, A., Walker, T.D., Christian, H.J., da Silva, C.L., Austin, M., Aguirre, F., Rassoul, H.K., 2021. Vertical temperature profile of natural lightning return strokes derived from optical spectra. J. Geophys. Res.: Atmos. 126, e2020JD034438 https://doi.org/10.1029/2020JD034438.
- Carvalho, F.L., Jordan, D.M., Uman, M.A., Ngin, T., Gamerota, W.R., Pilkey, J.T., 2014. Simultaneously measured lightning return stroke channel-base current and luminosity. Geophys. Res. Lett. 41, 7799–7805. https://doi.org/10.1002/ 2014GL062190.
- Carvalho, F.L., Uman, M.A., Jordan, D.M., Ngin, T., 2015. Lightning current and luminosity at and above channel bottom for return strokes and M-components. J. Geophys. Res. 120, 10645–10663. https://doi.org/10.1002/2015JD023814.
- Carvalho, F.L., Uman, M.A., Jordan, D.M., Wilkes, R.A., Kotovsky, D.A., 2018. Triggered lightning return stroke luminosity up to 1 km in two optical bands. J. Geophys. Res.: Atmos. 123, 9724–9740. https://doi.org/10.1029/2018JD028644.
- Christian, H.J., Blakeslee, R.J., Boccippio, D.J., Boeck, W.L., Buechler, D.E., Driscoll, K. T., Goodman, S.J., Hall, J.M., Koshak, W.J., Mach, D.M., Stewart, M.F., 2003. Global frequency and distribution of lightning as observed from space by the Optical Transient Detector. J. Geophys. Res. 108, ACL 4-1–ACL 4-15. https://doi.org/10.1029/2002JD002347.
- Cressault, Y., Bauchire, J.M., Hong, D., Rabat, H., Riquel, G., Sanchez, F., Gleizes, A., 2015. Radiation of long and high power arcs. J. Phys. D Appl. Phys. 48, 415201 https://doi.org/10.1088/0022-3727/48/41/415201.
- Ding, Z., Rakov, V., 2022. Toward a better understanding of negative lightning stepped leaders. Electr. Power Syst. Res. 209, 108043 https://doi.org/10.1016/j. epsr.2022.108043.

- Ding, Z., Rakov, V.A., Zhu, Y., Tran, M.D., 2020. On a possible mechanism of reactivation of decayed branches of negative stepped leaders. J. Geophys. Res.: Atmos. 125, e2020JD033305 https://doi.org/10.1029/2020JD033305.
- Ding, Z., Rakov, V.A., Zhu, Y., Tran, M.D., Kostinskiy, A.Y., Kereszy, I., 2021. Evidence and inferred mechanism of collisions of downward stepped-leader branches in negative lightning. Geophys. Res. Lett. 48, e2021GL093295 https://doi.org/ 10.1029/2021GL093295.
- Goodman, S.J., Blakeslee, R.J., Koshak, W.J., Mach, D., Bailey, J., Buechler, D., Carey, L., Schultz, C., Bateman, M., McCaul, E., Stano, G., 2013. The GOES-R Geostationary Lightning Mapper (GLM). Atmos. Res. 125–126, 34–49. https://doi.org/10.1016/j.atmosres.2013.01.006
- Guo, C., Krider, E.P., 1982. The optical and radiation field signatures produced by lightning return strokes. J. Geophys. Res.: Oceans 87, 8913–8922. https://doi.org/ 10.1029/JC087iC11p08913.
- Jordan, D.M., Uman, M.A., 1983. Variation in light intensity with height and time from subsequent lightning return strokes. J. Geophys. Res.: Oceans 88, 6555–6562. https://doi.org/10.1029/JC088iC11p06555.
- Kieu, N., Gordillo-Vazquez, G., Passas, M., Sanchez, J., Perez-Invernon, F., 2021. High-speed spectroscopy of lightning-like discharges: Evidence of molecular optical emissions. J. Geophys. Res. Atmos. 126, e2021JD035016 https://doi.org/10.1029/2021JD035016
- Koshak, W.J., Solakiewicz, R.J., Phanord, D.D., Blakeslee, R.J., 1994. Diffusion model for lightning radiative transfer. J. Geophys. Res. Atmos. 99, 14361–14371. https://doi. org/10.1029/94JD00022.
- Krider, E.P., 1992. On the electromagnetic fields, poynting vector, and peak power radiated by lightning return strokes. J. Geophys. Res.: Atmos. 97, 15913–15917. https://doi.org/10.1029/92JD01490.
- Krider, E.P., Dawson, G.A., Uman, M.A., 1968. Peak power and energy dissipation in a single-stroke lightning flash. J. Geophys. Res. 1896–1977 (73), 3335–3339. https://doi.org/10.1029/JB073i010p03335.
- Laux, C., Gessman, R., Hilbert, B., Kruger, C., 1995. Experimental study and modeling of infrared air plasma radiation. pp. 2124. doi: 10.2514/6.1995-2124.
- Liu, F., Lu, G., Neubert, T., Lei, J., Chanrion, O., Østgaard, N., Li, D., Luque, A., Gordillo-Vázquez, F.J., Reglero, V., Lyu, W., Zhu, B., 2021. Optical emissions associated with narrow bipolar events from thunderstorm clouds penetrating into the stratosphere. Nat. Commun. 12, 6631. https://doi.org/10.1038/s41467-021-26914-4.
- Luque, A., Gordillo-Vázquez, F.J., Li, D., Malagón-Romero, A., Pérez-Invernón, F.J., Schmalzried, A., Soler, S., Chanrion, O., Heumesser, M., Neubert, T., Reglero, V., Østgaard, N., 2020. Modeling lightning observations from space-based platforms (CloudScat.jl 1.0). Geosci. Model Dev. 13, 5549–5566. https://doi.org/10.5194/ gmd-13-5549-2020.
- Neubert, T., Østgaard, N., Reglero, V., Blanc, E., Chanrion, O., Oxborrow, C.A., Orr, A., Tacconi, M., Hartnack, O., Bhanderi, D.D.V., 2019. The ASIM mission on the International Space Station. Space Sci. Rev. 215, 26. https://doi.org/10.1007/s11214-019-0592-z.
- Orville, R.E., Henderson, R.W., 1984. Absolute spectral irradiance measurements of lightning from 375 to 880 nm. J. Atmos. Sci. 41, 3180–3187. https://doi.org/10.1175/1520-0469(1984)041<3180:ASIMOL>2.0.CO;2.
- Orville, R.E., Uman, M.A., 1965. The optical continuum of lightning. J. Geophys. Res. 70, 279–282. https://doi.org/10.1029/JZ070i002p00279.
- Paxton, A.H., Gardner, R.L., Baker, L., 1986. Lightning return stroke. A numerical calculation of the optical radiation. Phys. Fluids 29, 2736–2741. https://doi.org/ 10.1063/1.865514.
- Pérez-Invernón, F.J., Gordillo-Vázquez, F.J., Passas-Varo, M., Neubert, T., Chanrion, O., Reglero, V., Østgaard, N., 2022. Multispectral optical diagnostics of lightning from space. Remote Sens. 14, 2057. https://doi.org/10.3390/rs14092057.
- Quick, M.G., Krider, E.P., 2013. Optical power and energy radiated by natural lightning. J. Geophys. Res.: Atmos. 118, 1868–1879. https://doi.org/10.1002/jgrd.50182.
- Quick, M.G., Krider, P.E., 2017. Optical power and energy radiated by return strokes in rocket-triggered lightning. J. Geophys. Res. 122, 8816–8832. https://doi.org/ 10.1002/2017.JD027363.
- Rison, W., Krehbiel, P.R., Stock, M.G., Edens, H.E., Shao, X.M., Thomas, R.J., Stanley, M. A., Zhang, Y., 2016. Observations of narrow bipolar events reveal how lightning is initiated in thunderstorms. Nat. Commun. 7 https://doi.org/10.1038/ncomms10721
- Siegel, R., 2001. Thermal radiation heat transfer, fourth ed., vol. 1. CRC press, New York. da Silva, C.L., Pasko, V.P., 2013. Dynamics of streamer-to-leader transition at reduced air densities and its implications for propagation of lightning leaders and gigantic jets. J. Geophys. Res. 118, 13561–13590. https://doi.org/10.1002/2013JD020618.
- da Silva, C.L., Sonnenfeld, R.G., Edens, H.E., Krehbiel, P.R., Quick, M.G., Koshak, W.J., 2019. The plasma nature of lightning channels and the resulting nonlinear resistance. J. Geophys. Res. 124, 9442–9463. https://doi.org/10.1029/ 2019.07920632
- Soler, S., Pérez-Invernón, F.J., Gordillo-Vázquez, F.J., Luque, A., Li, D., Malagón-Romero, A., Neubert, T., Chanrion, O., Reglero, V., Navarro-Gonzalez, J., Lu, G., Zhang, H., Huang, A., Østgaard, N., 2020. Blue optical observations of narrow bipolar events by ASIM suggest corona streamer activity in thunderstorms. J. Geophys. Res. Atmos. 125, e2020JD032708 https://doi.org/10.1029/2020JD032708.
- Taylor, M.C., da Silva, C.L., Walker, T.D., Christian, H.J., 2022. Data-constrained simulations of the lightning return stroke channel properties. IEEE Trans. Electromag. Compat. 64, 1461–1469. https://doi.org/10.1109/TEMC.2022.3189500
- Traub, W.A., Stier, M.T., 1976. Theoretical atmospheric transmission in the mid- and far-infrared at four altitudes. Appl. Opt. 15, 364–377. https://doi.org/10.1364/ AO.15.000364

- $\label{lem:uman, M., 1963. The continuum spectrum of lightning. J. Atmos. Solar-Terr. Phys. 25, 287–295.$ <math display="block"> https://doi.org/10.1016/0021-9169(63)90025-4.
- Walker, T.D., Christian, H.J., 2017. Triggered lightning spectroscopy: Part 1. A qualitative analysis. J. Geophys. Res. 122, 8000–8011. https://doi.org/10.1002/2016.ID026419
- 2016JD026419.

 Walker, T.D., Christian, H.J., 2019. Triggered lightning spectroscopy: 2. A quantitative analysis. J. Geophys. Res. 124, 3930–3942. https://doi.org/10.1029/2018_ID029901
- Weidman, C., Boye, A., Crowell, L., 1989. Lightning spectra in the 850- to 1400-nm near-infrared region. J. Geophys. Res. Atmos. 94, 13249–13257. https://doi.org/10.1029/JD094iD11p13249.
- Zhou, M., Wang, D., Wang, J., Takagi, N., Gamerota, W.R., Uman, M.A., Jordan, D.M., Pilkey, J.T., Ngin, T., 2014. Correlation between the channel-bottom light intensity and channel-base current of a rocket-triggered lightning flash. J. Geophys. Res. 119, 13457–13473. https://doi.org/10.1002/2014JD022367.